CATALYSIS

First-principles design of a single-atom–alloy propane dehydrogenation catalyst

Ryan T. Hannagan[1]†, Georgios Giannakakis[2]†, Romain Réocreux[3]†, Julia Schumann[3,4,5], Jordan Finzel[6], Yicheng Wang[1], Angelos Michaelides[4,5], Prashant Deshlahra[2], Phillip Christopher[6], Maria Flytzani-Stephanopoulos[2], Michail Stamatakis[3]*, E. Charles H. Sykes[1]*

The complexity of heterogeneous catalysts means that a priori design of new catalytic materials is difficult, but the well-defined nature of single-atom–alloy catalysts has made it feasible to perform unambiguous theoretical modeling and precise surface science experiments. Herein we report the theory-led discovery of a rhodium-copper (RhCu) single-atom–alloy catalyst for propane dehydrogenation to propene. Although Rh is not generally considered for alkane dehydrogenation, first-principles calculations revealed that Rh atoms disperse in Cu and exhibit low carbon-hydrogen bond activation barriers. Surface science experiments confirmed these predictions, and together these results informed the design of a highly active, selective, and coke-resistant RhCu nanoparticle catalyst that enables low-temperature nonoxidative propane dehydrogenation.

Despite their widespread prevalence in industry, the improvement of heterogeneous catalysts is usually an empirical process, and examples of rational design remain extremely rare (*1*, *2*). Rational design is impeded in part by the enormous complexity of most heterogeneous catalysts, which often consist of metal nanoparticles (NPs) that expose a wide range of active sites with which the reactants can interact and react (*3*). Metal NPs can also restructure under reaction conditions (*4*). One approach to reduce the complexity of metal NPs is to reduce the active site to a single atom (*5*, *6*). However, the heterogeneity of the oxide support and the adaptive nature of the local environment make rational design of even these materials challenging (*7*, *8*).

Single-atom alloys (SAAs), a subclass of single-atom catalysts, consist of a reactive dopant metal atomically dispersed in a second metal host (*9*). Many SAAs are active, selective, and robust for a wide variety of reactions because the thermodynamics of mixing favor the atomic dispersion of the dopant in the more inert but more selective host (*10*). Furthermore, the well-defined nature of the active sites in SAAs, which have been atomically resolved in both model and NP systems, makes it possible to unambiguously model their behavior with theory (*11*–*13*).

[1]Department of Chemistry, Tufts University, Medford, MA 02155, USA. [2]Department of Chemical and Biological Engineering, Tufts University, Medford, MA 02155, USA. [3]Thomas Young Centre and Department of Chemical Engineering, University College London, Roberts Building, Torrington Place, London WC1E 7JE, UK. [4]Yusuf Hamied Department of Chemistry, University of Cambridge, Lensfield Road, CB2 1EW Cambridge, UK. [5]Department of Physics and Astronomy, University College London, Gower Street, London WC1E 6BT, UK. [6]Department of Chemical Engineering, University of California, Santa Barbara, CA 93106, USA.
***Corresponding author. Email: m.stamatakis@ucl.ac.uk (M.S.); charles.sykes@tufts.edu (E.C.H.S.)**
†These authors contributed equally to this work.

Guided by theoretical predictions, we present the rational design of a RhCu SAA catalyst for nonoxidative propane dehydrogenation to two valuable compounds: propene and hydrogen (*14*). Our theoretical screening of SAA combinations for this reaction began by examining C–H activation of methane, which is the simplest probe molecule for establishing trends in C–H activation. We used density functional theory (DFT) to determine (i) the activation energy of the first C–H scission and (ii) the segregation energy, which reflects the propensity of the dopant atom to migrate from the surface layer to the bulk of the host metal (see computational details in the supplementary materials). Of all SAA combinations screened, the Rh-doped alloys have the lowest C–H activation energies (Fig. 1A and figs. S1 to S3). In fact, these C–H activation energies are similar to those of pure transition metals (Pt and Rh) and the industrially relevant $Pt_3Sn(111)$ (2 × 2) intermetallic alloy (Fig. 1 and fig. S3) (*15*). However, of the three Rh-doped SAAs, RhCu (111) has the most favorable mixing enthalpy and segregation energy when reaction intermediates are present (Fig. 1A and figs. S1 and S2) (*16*). Specific to the mixing enthalpy, the energy change associated with isolated Rh atoms in a Cu(111) surface forming a dimer or a trimer is positive (>0.16 eV), indicating that the thermodynamic stability of single Rh atoms is greater than that of Rh clusters in a Cu host, which makes RhCu a promising SAA catalyst (*16*).

Comparison of the geometric and electronic structures of adsorbed methane on the SAA provided insight into the magnitude of the C–H activation barriers (Fig. 1B and fig. S4). On the RhCu(111) SAA surface, methane adsorbed 0.35 Å closer to the dopant atom than on pure Cu(111) (tables S1 and S2). This shorter distance increased the charge density difference $\Delta\rho(\mathbf{r})$ upon adsorption (Fig. 1B and fig. S4) by moving part of the electronic density from the C–H internuclear region to the H···Rh internuclear region. This electronic redistribution is prominent on the RhCu(111) SAA and is observed on pure Pt(111) but is negligible on Cu(111). For the former two materials, this electronic redistribution is indicative of the preactivation of methane upon adsorption (*17*).

After identifying the RhCu(111) SAA as the most promising candidate for C–H activation, we calculated the energy profile for the full dehydrogenation of methane to atomic carbon on the RhCu(111) SAA, the bare Cu(111) surface, and Pt(111), one of the most effective metals for C–H activation reactions (Fig. 1C and fig. S3). Notably, the single Rh atom in the RhCu(111) SAA had an almost identical activation energy to that of pure Pt(111). However, unlike pure Pt(111), which stabilized $CH_{2(ads)}$, $CH_{(ads)}$, and $C_{(ads)}$ intermediates that lead to coking, the RhCu(111) SAA inherited much of the coke resistance of pure Cu(111), with coke formation

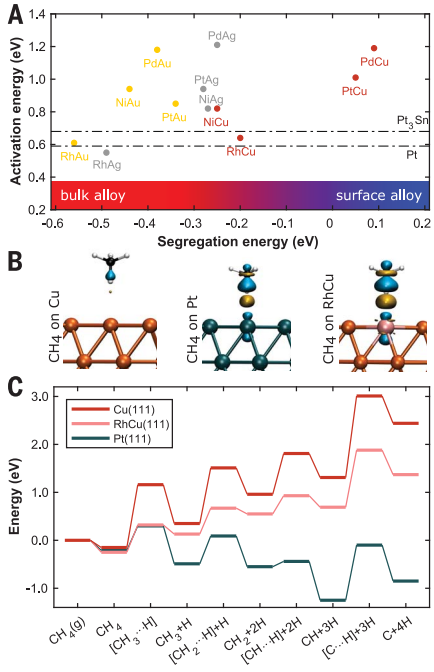

Fig. 1. Theoretical screening of SAA catalysts for C–H activation. (**A**) Activation energy of the first C–H cleavage in CH_4 plotted against segregation energy of each SAA. For comparison, the activation energies on Pt(111) and $Pt_3Sn(111)$ (2 × 2) are shown as dash-dotted lines. (**B**) Charge density difference $\Delta\rho(\mathbf{r})$ for adsorbed CH_4 on Cu(111), Pt(111), and RhCu(111) SAA. Orange, Cu atoms; teal, Pt atoms; pink, Rh atoms. Cyan and yellow contours represent regions of electron depletion and accumulation, respectively (isovalue of ±0.01 electron $Å^{-3}$). (**C**) Energy profile of the sequential C–H activation steps of CH_4 on various metal surfaces (more details in fig. S3). The energy is referenced with respect to the clean slab and $CH_{4(g)}$. H atoms are adsorbed on the Cu host metal in the SAA case.

being exothermic on Pt(111) versus endothermic on pure Cu(111) and the RhCu(111) SAA (Fig. 1C). This is a notable result, given that Rh is generally not considered for dehydrogenation reactions because Rh NPs suffer from coking and hydrogenolysis is favored over selective dehydrogenation (*18*).

To test the theoretical predictions outlined above and investigate the individual reaction steps, we performed surface science and high-resolution imaging studies of model RhCu(111) SAA catalysts. Physical vapor deposition of Rh on a Cu(111) surface held at an elevated temperature yielded atomically dispersed Rh atoms that substituted Cu atoms in the surface layer (*19*). A typical image of the SAA surface is shown in fig. S5. Given the low desorption barrier of methane relative to typical C–H activation barriers, we used methyl iodide (CH_3I) as a probe molecule to study C–H activation in adsorbed methyl groups on the model RhCu(111) SAA surfaces. Specifically, C–I bond cleavage was facile on Cu(111), yielding methyl groups [$CH_{3(ads)}$] at low temperature that remained on the surface as it was heated. Once the rate-determining C–H activation step (RDS) occurred, yielding $H_{(ads)}$ and $CH_{2(ads)}$, gaseous methane evolved rapidly from facile coupling of $H_{(ads)}$ and $CH_{3(ads)}$, as described below (*20*)

$$CH_3I_{(ads)} \xrightarrow{fast} CH_{3(ads)} + I_{(ads)}$$

$$CH_{3(ads)} \xrightarrow{RDS} CH_{2(ads)} + H_{(ads)}$$

$$CH_{3(ads)} + H_{(ads)} \xrightarrow{fast} CH_{4(g)}$$

In this sense, methane evolution acted as a reporter of C–H activation, with lower-temperature methane evolution being associated with more facile C–H bond activation. Furthermore, the C–H activation barrier in CH_3 groups can be related to the C–H activation barrier in CH_4 via scaling relationships (fig. S6).

Temperature-programmed desorption (TPD) experiments on Cu(111) showed that C–H activation occurred at ~430 K (Fig. 2A), consistent with previous results (*20*). This finding was also consistent with our DFT calculations, which predicted that $CH_{3(ads)}$ conversion to $CH_{2(ads)}$ on Cu(111) had a barrier of 1.16 eV (Fig. 1C and fig. S3). Increasing the step density of the Cu(111) surface through argon ion sputtering resulted in a slightly lower C–H activation barrier and methane evolution at ~380 K. When individual, isolated Rh atoms were present in the Cu(111) surface, as seen in the low-temperature scanning tunneling microscopy (LT-STM) image and corresponding DFT-based image simulation in Fig. 2, B and C, several low-temperature methane evolution peaks were observed in the TPD experiments.

The lowest-temperature feature at ~160 K is caused by hydrogenation of methyl groups by hydrogen from the chamber background that dissociates at Rh sites. This result was confirmed by experiments in which we precovered the RhCu(111) SAA surface with hydrogen before CH_3I was introduced. This low-temperature methane peak arose due to the aforementioned facile $CH_{3(ads)} + H_{(ads)} \rightarrow CH_{4(g)}$ reaction (Fig. 2A, bottom trace). The next TPD feature, at ~300 K, was caused by C–H activation of the methyl groups to form $CH_{2(ads)}$ and $H_{(ads)}$, followed by hydrogenation of the remaining methyl fragments. The temperatures at which these reaction steps occurred were consistent with our DFT calculations, which yielded a barrier for C–H activation in CH_3 on the RhCu(111) SAA of 0.54 eV, in contrast to the facile hydrogenation of CH_3 to CH_4, which has a barrier of 0.19 eV (Fig. 1C and fig. S3). Finally, the smaller CH_4 desorption feature at ~350 K is consistent with reaction at Cu step sites that were created when Rh was alloyed with Cu(111) (*19*). Full TPD traces for each experiment are provided in the supplementary materials (fig. S7).

To track the progression of the reaction intermediates not observable by TPD, we conducted LT-STM experiments after exposing a RhCu(111) SAA to CH_3I and annealing to different temperatures before 5 K STM imaging (Fig. 2, D to G). After annealing to ~160 K, we observed the formation of small clusters of intact CH_3I (Fig. 2D). Heating to ~240 K resulted in dissociation of the C–I bond and $\sqrt{3} \times \sqrt{3}$ structural ordering of the $CH_{3(ads)}$ groups and $I_{(ads)}$ atoms seen in the STM images as protrusions [$I_{(ads)}$] and depressions [$CH_{3(ads)}$], confirming the facile C–I cleavage. At ~320 K, a substantial fraction of the methyl groups react and desorb as CH_4, and after a ~440 K anneal, only two-dimensional islands of I atoms (bright protrusions) in a $\sqrt{3} \times \sqrt{3}$ structure remain (*21*, *22*). Notably, the image in Fig. 2G reveals that, aside from I atoms, which remained adsorbed on Cu(111) until ~840 K, there was no evidence of substantial coke formation, consistent with our theoretical predictions.

Guided by our theoretical calculations and surface science studies, we synthesized RhCu/SiO_2 NP catalyst analogs with a Rh:Cu ratio of 1:100, demonstrated that they are indeed SAAs, and then tested them for the nonoxidative dehydrogenation of propane. RhCu/SiO_2 NPs of ~3-nm diameter were synthesized through galvanic replacement of silica-supported copper NPs (figs. S8 and S9) by small amounts of

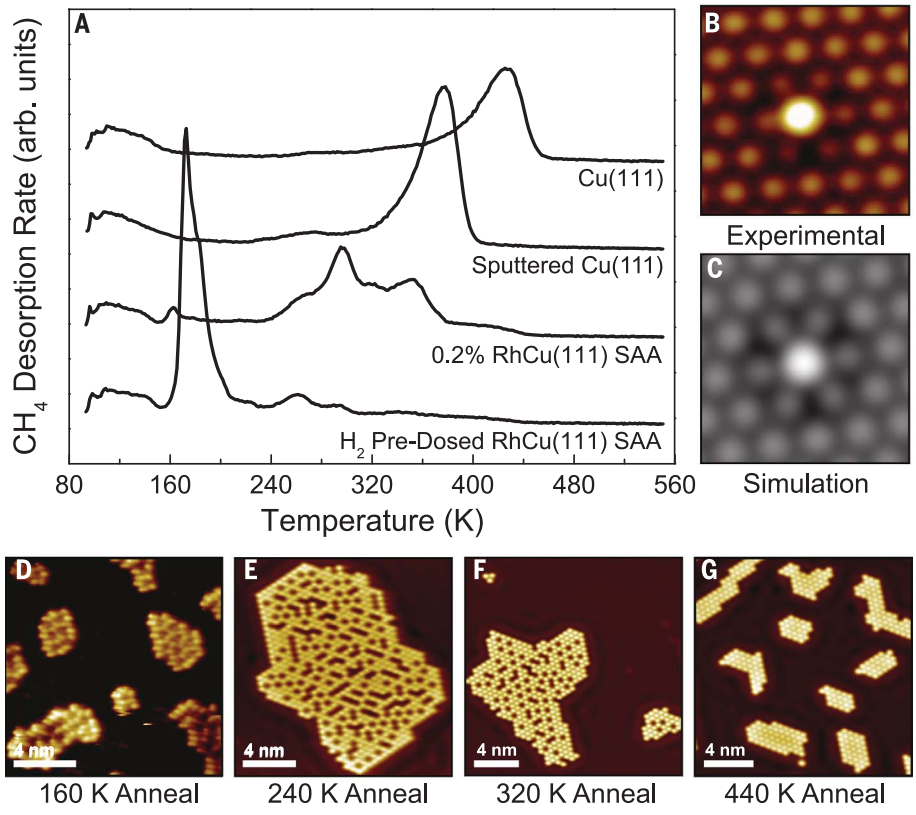

Fig. 2. Model system studies demonstrating that RhCu(111) SAAs promote low-temperature C–H activation. (**A**) TPD experiments on Cu(111), sputtered Cu(111), 0.2% RhCu(111) SAA, and 0.2% RhCu(111) SAA pre-dosed with 200 Langmuir [1 Langmuir (L) = 10^{-6} torr · s] of hydrogen. Each surface was exposed to 1.5 L of CH_3I. (**B**) STM image of an isolated Rh atom in Cu(111). (**C**) DFT-simulated STM image of an isolated Rh atom in Cu(111). (**D** to **G**) STM images from annealing experiments in which the RhCu(111) SAA was exposed to CH_3I, annealed to the indicated temperatures, and imaged at 5 K to track reaction progression.

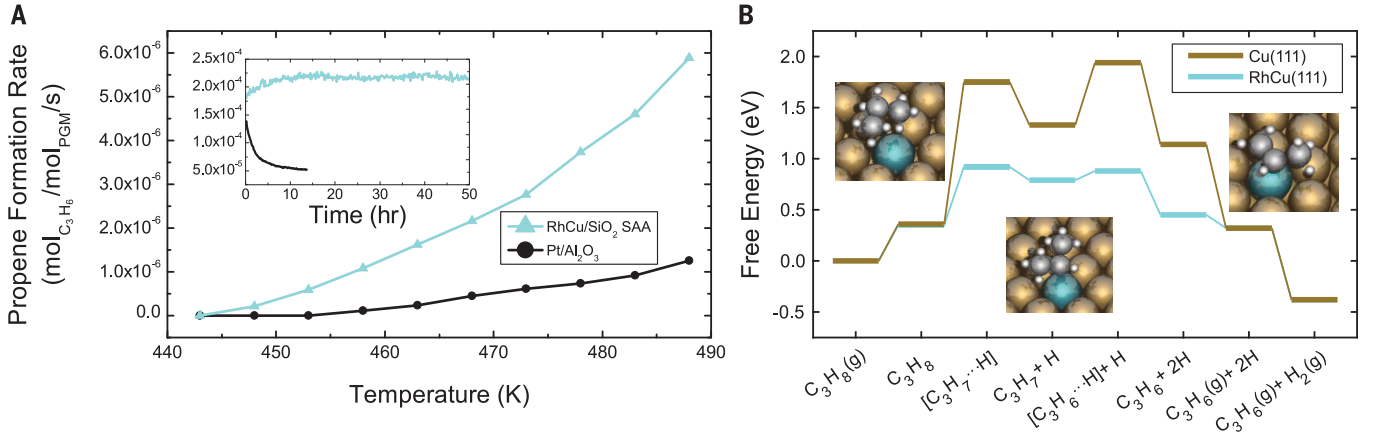

Fig. 3. Propane dehydrogenation on RhCu SAAs. (**A**) Propene formation rate versus temperature for the nonoxidative propane dehydrogenation reaction on $RhCu/SiO_2$ SAA (Rh:Cu 1:100) and Pt/Al_2O_3 catalysts. (Inset) Stability test (50 hours) of $RhCu/SiO_2$ SAA versus Pt/Al_2O_3 at 623 K. Gas composition: 1.4 kPa of propane and 0.7 kPa of hydrogen; 90-ml-per-min flow rate. Formation rate was normalized per mole of platinum-group metal (PGM). (**B**) Free-energy diagram of RhCu(111) SAA and Cu(111) for the nonoxidative dehydrogenation of propane. Free energies were calculated at 500 K for a C_3H_8 and H_2 partial pressure of 1 kPa and a C_3H_6 partial pressure of 0.01 Pa. The energies are referenced with respect to the clean slabs and C_3H_8(g). H refers to a H atom adsorbed on the Cu metal surface.

Rh (*10*). CO diffuse reflectance infrared Fourier transform spectroscopy (DRIFTS) and in situ extended x-ray absorption fine structure (EXAFS) studies were performed to verify the successful alloying, as well as the absence of surface Rh aggregates. DRIFTS results (figs. S10 and S11) revealed a narrow (~15 cm^{-1} full width at half maximum) peak corresponding to linear CO adsorption on Rh atoms at 2089 cm^{-1}. Notably, no infrared signals for Rh directly on SiO_2 or Rh aggregates at the Cu surface were observed (*23*, *24*), thereby demonstrating that a SAA was formed, in line with our EXAFS analysis (figs. S12 and S13 and table S3).

We tested the $RhCu/SiO_2$ SAA catalyst for propane dehydrogenation in flow-reactor studies away from equilibrium in the kinetic regime. We performed a direct comparison of the $RhCu/SiO_2$ SAA catalyst with a standard consisting of Pt NPs supported on Al_2O_3 (*25*). Experiments were conducted both in the absence (fig. S14) and presence (Fig. 3A) of hydrogen in the feed (the latter experiment was performed to better simulate industrially relevant conditions in which a co-flow of H_2 is required to prevent Pt from coking). The data in Fig. 3A revealed that the $RhCu/SiO_2$ SAA catalyst exhibited higher activity per mole of active metal, as well as a considerably lower reaction light-off temperature, than Pt/Al_2O_3.

The high reactivity of the $RhCu/SiO_2$ SAA catalyst was coupled with Cu-like propene selectivity (100% on $RhCu/SiO_2$ SAA versus ~80% on Pt/Al_2O_3) and resistance to coking (fig. S15 and table S4). Although pure Rh NPs are poor dehydrogenation catalysts that are susceptible to coking because of the strong binding of carbon to extended Rh sites (*18*, *26*), the atomic dispersion of Rh in our SAA catalysts enabled facile C–H activation while avoiding over-dehydrogenation that leads to coke formation by virtue of the endothermic nature of the coking process on single Rh atoms in a Cu host (Fig. 1C and fig. S3). This coking resistance resulted in the active, selective, and stable conversion of propane to propene and hydrogen for more than 50 hours on stream at 623 K (Fig. 3A, inset).

To further understand these experimental observations, we used DFT to calculate and compare the propane dehydrogenation reaction energetics of the RhCu(111) SAA to those of pure Cu(111), Rh(111), and Pt(111). Our DFT calculations (Fig. 3B, figs. S16 and S17, and table S5) show that the RhCu(111) SAA surface provided lower thermodynamic barriers for the formation of the isopropyl intermediate and propene than the pure Cu(111) surface. In addition, relative to Cu(111), the SAA exhibited a considerably lower kinetic barrier for the first dehydrogenation step [0.57 eV on the RhCu(111) SAA versus 1.39 eV on Cu(111)] and a very small subsequent kinetic barrier for the C_3H_7-to-C_3H_6 step (0.10 eV), indicative of a highly active catalyst. Notably, the activation barrier of propane on the RhCu(111) SAA is lower than that on pristine Pt(111) and very similar to that on Rh(111) [0.68 and 0.63 eV, respectively (fig. S16 and table S5)]. These results are consistent with experimental observations in which we measured the rate of propane dehydrogenation on the $RhCu/SiO_2$ SAA catalyst away from equilibrium over a small temperature window and found an apparent activation energy of ~0.7 eV (fig. S18). The measured apparent activation energy was identical with and without H_2, which suggests that there was not a substantial coverage of H on the catalyst surface at these temperatures.

One potential limitation in the widespread application of RhCu SAA catalysts is the well-known sintering of Cu NPs at elevated temperatures. However, despite the expected loss of reactivity because of the sintering of Cu NPs (*27*), measurements of the initial propane dehydrogenation rates performed at 773 K showed that the $RhCu/SiO_2$ SAA catalyst performed comparably to other Pt-based catalysts previously reported (table S6) (*28*). Furthermore, we observed that addition of 1% Rh to the Cu NPs provided them with enhanced sintering resistance relative to pure Cu NPs (fig. S8). Methods known to stabilize metal NPs against sintering at high temperatures, such as atomic layer deposition of thin oxide layers, could further address this issue (*29*).

REFERENCES AND NOTES

1. F. Besenbacher *et al.*, *Science* **279**, 1913–1915 (1998).
2. S. Alayoglu, A. U. Nilekar, M. Mavrikakis, B. Eichhorn, *Nat. Mater.* **7**, 333–338 (2008).
3. R. van Lent *et al.*, *Science* **363**, 155–157 (2019).
4. F. Tao *et al.*, *Science* **322**, 932–934 (2008).
5. B. Qiao *et al.*, *Nat. Chem.* **3**, 634–641 (2011).
6. B. C. Gates, M. Flytzani-Stephanopoulos, D. A. Dixon, A. Katz, *Catal. Sci. Technol.* **7**, 4259–4275 (2017).
7. J. Hulva *et al.*, *Science* **371**, 375–379 (2021).
8. L. DeRita *et al.*, *Nat. Mater.* **18**, 746–751 (2019).
9. G. Kyriakou *et al.*, *Science* **335**, 1209–1212 (2012).
10. R. T. Hannagan, G. Giannakakis, M. Flytzani-Stephanopoulos, E. C. H. Sykes, *Chem. Rev.* **120**, 12044–12088 (2020).
11. M. T. Darby, M. Stamatakis, A. Michaelides, E. C. H. Sykes, *J. Phys. Chem. Lett.* **9**, 5636–5646 (2018).
12. G. Giannakakis, M. Flytzani-Stephanopoulos, E. C. H. Sykes, *Acc. Chem. Res.* **52**, 237–247 (2019).
13. M. T. Darby, R. Réocreux, E. C. H. Sykes, A. Michaelides, M. Stamatakis, *ACS Catal.* **8**, 5038–5050 (2018).
14. National Academies of Sciences, Engineering, and Medicine, *The Changing Landscape of Hydrocarbon Feedstocks for Chemical Production: Implications for Catalysis: Proceedings of a Workshop* (The National Academies Press, 2016).
15. D. Gerceker *et al.*, *ACS Catal.* **7**, 2088–2100 (2017).
16. M. T. Darby, E. C. H. Sykes, A. Michaelides, M. Stamatakis, *Top. Catal.* **61**, 428–438 (2018).
17. V. Fung, G. Hu, B. Sumpter, *J. Mater. Chem. A* **8**, 6057–6066 (2020).
18. J. H. Sinfelt, D. J. C. Yates, *J. Catal.* **8**, 82–90 (1967).
19. R. T. Hannagan *et al.*, *ChemCatChem* **12**, 488–493 (2019).
20. C. Chao-Ming, B. E. Bent, *Surf. Sci.* **279**, 79–88 (1992).
21. M. Pascal *et al.*, *Surf. Sci.* **512**, 173–184 (2002).
22. M. D. Marcinkowski *et al.*, *Nat. Chem.* **10**, 325–332 (2018).

23. S. Gonzalez, C. Sousa, F. Illas, *Int. J. Mod. Phys. B* **24**, 5128–5138 (2010).
24. J. A. Anderson, C. H. Rochester, Z. Wang, *J. Mol. Catal. Chem.* **139**, 285–303 (1999).
25. J. J. H. B. Sattler, J. Ruiz-Martinez, E. Santillan-Jimenez, B. M. Weckhuysen, *Chem. Rev.* **114**, 10613–10653 (2014).
26. N. Raman *et al*., *ACS Catal.* **9**, 9499–9507 (2019).
27. M. V. Twigg, M. S. Spencer, *Top. Catal.* **22**, 191–203 (2003).
28. G. Sun *et al*., *Nat. Commun.* **9**, 4454 (2018).
29. B. J. O'Neill *et al*., *Angew. Chem. Int. Ed.* **52**, 13808–13812 (2013).

ACKNOWLEDGMENTS

R.T.H. would like to acknowledge useful conversations with P. Kress. G.G. would like to thank A. Clark and P. Cebe for help with thermogravimetric analysis measurements. M.S. and R.R. acknowledge M. Mavrikakis for providing the Pt_3Sn slab for the DFT calculation. **Funding:** R.T.H., Y.W., and E.C.H.S. acknowledge funding from the Division of Chemical Science, Office of Basic Energy Science, CPIMS Program, US Department of Energy, under grant DE-SC 0004738. G.G. was supported in part by the Integrated Mesoscale Architectures for Sustainable Catalysis, an Energy Frontier Research Center funded by the US Department of Energy, Office of Science, Basic Energy Sciences, under award DE-SC0012573. R.R., M.S., and A.M. acknowledge funding from the Leverhulme Trust, grant RPG-2018-209. J.S. is supported by the Alexander von Humboldt Foundation, Germany, through a Feodor Lynen Fellowship. J.F. acknowledges support from NSF GRFP. P.C. acknowledges support from DOE BES DE-SC0021124. P.D. acknowledges support from the National Science Foundation (award 2034911). R.R., J.S., A.M., and M.S. thank the UK Materials and Molecular Modelling Hub, which is partially funded by EPSRC (EP/PO20194/1 and EP/T022213/1); the HEC Materials Chemistry Consortium, which is funded by EPSRC (EP/L000202); and the UCL Research Computing Services for computational resources. High-angle annular dark-field–scanning transmission electron microscopy and x-ray fluorescence measurements made use of the MRL Shared Experimental Facilities, which are supported by the MRSEC Program of the NSF (under award DMR 1720256), a member of the NSF-funded Materials Research Facilities Network (www.mrfn.org). **Author contributions:** R.T.H. performed the surface science experiments and wrote the initial draft. G.G. performed the catalysts synthesis and testing. R.R. and J.S. carried out the theoretical calculations. Y.W. and J.F. did the microscopy, and J.F. analyzed the x-ray absorption data. A.M., P.D., P.C., M.F.-S., M.S., and E.C.H.S. were responsible for supervision, analysis, editing, and funding acquisition. **Competing interests:** Tufts University has submitted a provisional patent entitled "A Rhodium/Copper Single-Atom Alloy Heterogeneous Catalyst for the Dehydrogenation of Alkanes" on which R.T.H., G.G., and E.C.H.S. are listed as inventors (US provisional patent number 63/201,784). The authors declare no other competing interests. **Data and materials availability:** All data are available in the main text or the supplementary materials.

SUPPLEMENTARY MATERIALS

5 February 2021; accepted 18 May 2021
10.1126/science.abg8389

First-principles design of a single-atom–alloy propane dehydrogenation catalyst

Ryan T. Hannagan, Georgios Giannakakis, Romain Réocreux, Julia Schumann, Jordan Finzel, Yicheng Wang, Angelos Michaelides, Prashant Deshlahra, Phillip Christopher, Maria Flytzani-Stephanopoulos, Michail Stamatakis, and E. Charles H. Sykes

Science **372** (6549), . DOI: 10.1126/science.abg8389

Rhodium atoms for alkane dehydrogenation

Nanoparticles of rhodium dispersed on metal oxides are generally poor catalysts for alkane dehydrogenation because the reactants bind too strongly to the metal. Hannagan *et al.* performed first-principle calculations indicating that single rhodium atoms in a copper surface should be stable and selective for conversion of propane to propene and hydrogen. Model studies of single rhodium atoms embedded in a copper (111) surface revealed a very high selectivity to propene and high resistance to the formation of surface carbon that would deactivate the catalyst.

Science, abg8389, this issue p. 1444